Nuclear Instruments and Methods in Physics Research B 579 (2026) 166217

Contents lists available at ScienceDirect

Nuclear Inst. and Methods in Physics Research, B

journal homepage: www.elsevier.com/locate/nimb

Full length article

The voltage dependent transmission function of a retarding field analyzer

L. Assink [a,b], E. de Wit [a,b], F. Veen [a,b], K. Bijlsma [a,b], O.O. Versolato [b,c], R. Hoekstra [a,b,*]

[a] Zernike Institute for Advanced Materials, University of Groningen, Nijenborgh 3, 9747 AG, Groningen, The Netherlands
[b] Advanced Research Center for Nanolithography (ARCNL), Science Park 106, 1098 XG, Amsterdam, The Netherlands
[c] Department of Physics and Astronomy, and LaserLaB, Vrije Universiteit, De Boelelaan 1100, 1081 HV, Amsterdam, The Netherlands

ARTICLE INFO

Keywords:
RFA
Transmission
Plasma diagnostics
Faraday cup
IEDF

ABSTRACT

Retarding field analyzers (RFA) are widely used to measure ion energy distributions and fluxes from plasmas, but quantitative flux determination requires accurate knowledge of their grid stack transmission. The dependence of the transmission factor on the barrier voltage is investigated through a combination of experimental measurements and ion trajectory simulations. Experimental results for different ion species reveal a common transmission-voltage relationship independent of ion species, indicating that the effect is intrinsic to the analyzer. Ion trajectories through a four-grid RFA were modeled using SIMION to examine the influence of grid alignment and bias configuration. Without retarding potential, the transmission can be estimated by optical inspection. However, applied voltages introduce electrostatic lensing, which is most pronounced when grids are geometrically aligned. The electron suppressor grid introduces appreciable oscillations in transmission as a function of the voltage just below the ion cutoff voltage. The overall transmission arises from an intricate interplay of lensing, alignment, and grid spacing.

1. Introduction

The retarding field analyzer (RFA) is a compact and versatile instrument widely used to measure charged particle fluxes. Its ease of use and reliability have made it a standard tool for measuring ion energy distribution functions (IEDFs), particularly in the fields of plasma and ion beam physics [1–3]. One may think of (industrial) low-temperature plasma generators [4,5], thermonuclear fusion reactors [6–8], ion beam sources and interactions [9,10], spacecraft thrusters [11–14], and plasma sources for extreme ultraviolet (EUV) light for photolithography [15–17].

An RFA primarily consists of a Faraday cup (FC) to collect incoming ions (or electrons) and a stack of high-transmission grids (Fig. 1). The device owes its name to the retarding field that is created by applying a voltage to one of its electrodes. In this paper, we focus on ions, noting that the same principles apply to electrons with voltages of opposite polarity. The incoming ions are decelerated while passing through the field created by the retarding electrode. The potential on the retarding grid-electrode basically acts as a high-pass energy filter. It allows only ions with a kinetic energy E_{kin} greater than qV_R to overcome the potential barrier, where q is the charge state of the ion and V_R is the voltage set on the retarding electrode. Ions with insufficient energy are repelled. Differentiation of the measured current with respect to the retarding voltage yields the kinetic-energy distribution of the incoming ions.

The use of gridded electrodes aims to establish near-uniform potentials within the grid stack, thereby improving the energy resolution of the RFA. In practice, perfectly uniform potentials cannot be achieved due to field penetration within the electrodes, as discussed previously by Sakai [18]. However, the grids do intercept a significant fraction of the ions, reducing the measured current. Consequently, corrections are necessary to obtain quantitative ion fluxes from RFA measurements. Despite their wide use, a generic procedure for such corrections remains lacking and is recognized as a challenge in the absolute interpretation of RFA data [19–23].

A first-order correction for transmission losses is to scale the ion flux by the optical transmission value T, of the grid type used. Another widely used approach is the so-called "T^n" or "transmission multiplication rule", in which the optical transmission factors of all n individual grids are multiplied. The difference between these methods is substantial. As is evidenced by the comparison of the transmission values for an RFA with four identical grids of 81% transmission in either perfect alignment (i.e. only displaced along the optical axis) or all shifted with respect to one another. Assuming a parallel beam with no angular divergence, the transmission of the grid stack is 81% for perfect alignment of the four grids, while in the fully misaligned case, a transmission of 43% (0.81^4) is obtained. Throughout this work, this parallel beam transmission is referred to as the optical transmission.

* Corresponding author.
E-mail address: r.a.hoekstra@rug.nl (R. Hoekstra).

https://doi.org/10.1016/j.nimb.2026.166217
Received 23 February 2026; Received in revised form 5 June 2026; Accepted 5 June 2026
Available online 12 June 2026
0168-583X/

Table 1
Comparison between the grid geometry used in the present work and that investigated by Trottenberg et al. [23], including differences in aperture shape, spacing, single-grid transmission, symmetry, and relative grid orientation.

	This work	Trottenberg et al. [23]
Holes	Square	Circular
Hole side/diameter	229 µm	500 µm
Grid thickness	25.4 µm	200 µm
Single hole area	52.4×10^3 µm^2	196×10^3 µm^2
Hole–hole dist.	254 µm	700 µm
Transmission	81%	46%
Symmetry	4-fold	6-fold
Translation	Yes	No
Rotation	No	Yes

This represents a difference of nearly a factor of two, implying large uncertainties associated with the choice of the transmission correction method. Both approaches rely on simplified assumptions about the ion trajectories. The optical method assumes straight-line trajectories, while the multiplication method assumes a homogeneous ion flux across all grids. In reality, ions follow neither perfect straight-line trajectories nor uniform spatial distributions. Instead, their trajectories are influenced by the electrode potentials and the geometry of the grid stack, giving rise to electrostatic lensing effects. Such lensing behavior caused by nonuniform fields within a gridded RFA has previously been discussed by Klenzing et al. [24]. Such lensing can focus or deflect ion trajectories, potentially directing a larger fraction of ions onto one of the consecutive grids and thereby altering the fraction of ions intercepted. The magnitude of these lensing effects depends on the voltages applied to the electrodes. Consequently, the transmission factor is voltage-dependent, as will be demonstrated by our experiments and simulations with monoenergetic ion beams. These experiments and simulations will underline the necessity of considering setting-dependent RFA transmission functions.

Recent work by Trottenberg et al. [23] demonstrated that the relative orientation of drilled grids can strongly affect the measured transmission characteristics of an RFA, leading to pronounced non-monotonic features associated with ion focusing and "channeling" phenomena through aligned apertures. Their study considered a grid geometry consisting of circular apertures arranged in a hexagonal pattern, while in the present work square apertures arranged on a square lattice are investigated. The alignment of successive grids was changed either by relative grid rotation (Trottenberg et al. [23]), or in our case through lateral translation of the grids. In addition, the grid dimensions (hole size and area, grid thickness, and geometrical transmission) are clearly different between the two. A comparative list of RFA specifications is presented in Table 1. These specifications result in different symmetry and transparency of the grid systems used. Together, the two sets of works cover complementary aspects of the role of grid geometry and alignment effects on RFA transmission. It is of note that the ratio between hole side/diameter and the distance between consecutive grids is close to 0.1 for both cases. This quantity is a representative measure for field inhomogeneities [18].

In this work, the dependence of the transmission factor on the retarding voltage is investigated through a combination of experimental measurements and ion trajectory simulations. Experimental results reveal a transmission-voltage relationship which is the same for different ions beams, confirming that this behavior is an intrinsic characteristic of that RFA. To further explore this effect, ion trajectory simulations are performed for multiple grid configurations. The following section outlines the working principles of the RFA, emphasizing transmission and electrostatic lensing, after which the experimental setup and simulation approach are described.

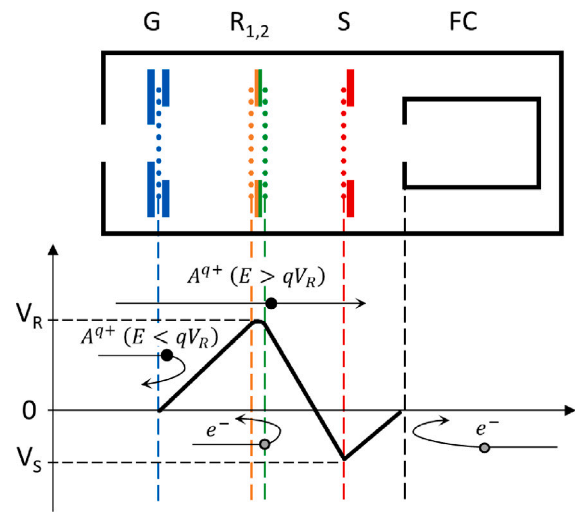

Fig. 1. Schematic of a four-grid retarding field analyzer. The retarding voltage V_R defines a potential barrier transmitting only ions above a threshold energy. A negative suppressor voltage V_S prevents both plasma and secondary electrons from entering or escaping the Faraday cup.

2. RFA working principles

This work is based on a four-grid retarding field analyzer equipped with a Faraday cup (FC) for ion collection. We focus specifically on a four-grid configuration, as it corresponds to the RFA used in our experimental measurements. The schematic and working principles of the instrument are shown in Fig. 1. Ions entering the RFA first pass through a grounded entrance grid (G) after which they encounter a set of two grids (R_1 and R_2) that together form the retarding electrode. The potential applied to these retarding grids defines the threshold energy for ions to reach the FC. Between the retarder and the collector, a suppressor grid (S) is placed that is biased negatively to serve two tasks: (i) to repel incoming plasma electrons and (ii) to prevent secondary electrons generated in the FC from escaping the FC.

The main function of the grids is to establish near-uniform electric fields between successive electrodes. This reduces unwanted effects on the ions' trajectories by field gradients stemming from specific, local electrode geometries, such as edges, holes, and connectors. Our grid stacks are commercial one by Kimball Physics (FC-73A), in which the retarding electrode has grids on either side of the retarding electrode plate. The use of a double-gridded retarding electrode aims to enhance the uniformity of the retarding barrier potential between the two grids with the goal of improving the energy resolution with respect to stacks with a single-grid retarding electrode. Nevertheless, ions flying through the center of a grid opening will experience a slightly different electric force compared to those passing close to the grid wires, e.g. Ref. [18].

Each grid effectively divides the beam into multiple smaller beamlets corresponding to ions passing through individual square apertures, cf. Figs. 2 and 4. These apertures act as weak electrostatic lenses that slightly deflect ion trajectories away from running parallel to the optical axis, introducing the electrostatic lensing effects. Depending on the specific grid configuration and applied potentials, these lensing effects can focus or defocus the beam, thereby modifying which ions are intercepted by subsequent grids. As a result, RFAs with identical optical transmissions may still exhibit different effective ion transmissions due to differences in grid configuration. Here, the term grid configuration refers to the relative positioning of the individual grids within the stack, including lateral shifts, relative rotations, and variations in the spacing between the successive grids. In this work, only lateral shifts are considered. Rotational shifts were previously investigated by Trottenberg et al. [23].

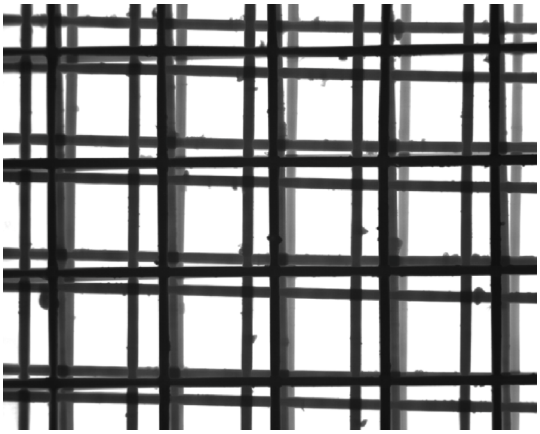

Fig. 2. The grid configuration of the four-grid RFA. Each grid was photographed separately with a CMOS camera (XIMEA MQ013MG-E2) due to the limited depth of field, and the images were subsequently overlaid to reconstruct the full configuration.

3. Research methods

3.1. Experimental setup

The ion beam experiments were performed in our crossed-beam setup [9,25], which is one of the two permanent stations at the ZERNIKELEIF low-energy ion beam facility at the University of Groningen. The ion beams are generated by a 14-GHz electron cyclotron resonance ion source (ECRIS), which can be operated on voltages up to 30 kV. Due to the internal plasma potential, the actual ion energy is approximately 15 eV/q (with q the charge state of the ion) [26] higher than the energy expected from the voltage set to the source. Typical beam energy spreads are 5 eV/q [26]. ECR ion sources are the workhorses for producing high-intensity, highly charged ion beams [27]. We mainly use the source to produce Sn ion beams to support our research on Sn ion interactions with matter, in the context of understanding and improving 13.5-nm EUV sources for photolithography [25,28]. After extraction from the ECRIS, the wished ion beam is selected using a 110° analyzing magnet with a mass-over-charge resolution of about 0.5%. The selected ion beam then enters a 10-m central beamline from which it is bent into the crossed-beam setup by means of a 45° bending magnet. On its way from the bending magnet to the gas target, the ion beam is collimated by a set of six apertures, of which the smallest two have a diameter of 1.5 mm. This limits the divergence of the beam to less than 1°. The base pressure in the beamline and station is approximately 1×10^{-8} mbar. Therefore, no appreciable traces of electron capture by the ions are observed in the RFA signals. The ion current is measured with a Keithley 6485 picoammeter.

3.2. Optical inspection of a grid stack

The optical transmission of the RFA grid stack was determined using shadowgraphy images taken with a CMOS camera (XIMEA MQ013MG-E2). Due to the camera's limited depth of field, each grid was imaged separately, and an overlay was constructed to visualize the complete grid stack (Fig. 2).

Binary images of individual grids were obtained by applying independent thresholds to correct for variations in image brightness and then combined to obtain the stack's transmission pattern. From these binary images, both the grid spacing and wire thickness were derived. The separations between the successive electrodes are 2.54 mm (0.1") between the G-grid and the R_1-grid, 0.635 mm (0.025") between the two retarding grids (R_1 and R_2), and 1.905 mm (0.075") between the R_2-grid and the S-grid. Each grid has 100 pitches per inch (0.254 mm pitch), and a wire diameter of 25.4 μm (0.001"), matching the single-grid transmission of 81%. The overlay analysis gives an overall optical transmission of 47%, slightly above the 43% expected from multiplicative stacking due to partial overlap of the grid wires (Fig. 2). These geometrical parameters will be used in the simulation models.

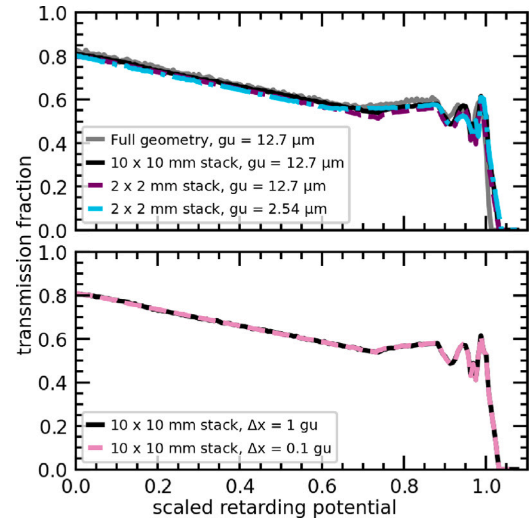

Fig. 3. Comparison between different numerical settings used in SIMION. The upper panel compares different simulation approaches using the complete enclosed geometry, the full grid-stack (10 × 10 mm), and high-resolution simulations with a spatial discretization of 2.54 μm per grid unit on a reduced grid stack geometry (2 × 2 mm). The lower panel compares the default trajectory integration step (Δx) of 1 grid unit to a reduced trajectory integration step of 0.1 grid unit.

3.3. Simulation approach

The simulations presented here are performed with the software package SIMION [29,30]. For all nine different grid configurations, the ion trajectories of a 4 keV He^{1+} ion beam flying through an RFA have been simulated by replacing the full geometry of the RFA with the grid stack alone. Prior to those calculations, simulations of the full-geometry of the RFA, including the surrounding shield and Faraday cup, were performed for four of these configurations. These calculations required specialized hardware with 128 GB of RAM and simulation times of several weeks per model. For this reason, we evaluated whether simulations restricted to the grid stack alone (10 × 10 mm) could accurately reproduce the behavior of the full geometry. As shown in the top panel of Fig. 3, excellent agreement between the two approaches is found.

As simulation grid size units in the model, we used 12.7 μm. This value was chosen such that grid wires are composed of two grid units, a minimum that is required by the software to define solid structures. The chosen resolution represents a compromise between numerical accuracy and computational feasibility, as increasing the spatial resolution rapidly leads to very large memory requirements and simulation times in SIMION. To assess the influence of discretization, additional simulations were performed for a higher spatial resolution of 2.54 μm per grid unit. The results of this discretization check are also included in the top panel of Fig. 3. No significant changes in the calculated transmission characteristics are found for the different approaches, indicating that using solely the grid-stack geometry is a valid approach.

As a further validity check, we tested the trajectory integration used by SIMION. We used its default setting, which corresponds to a nominal step length of 1 grid unit (12.7 μm) per integration step. For validation,

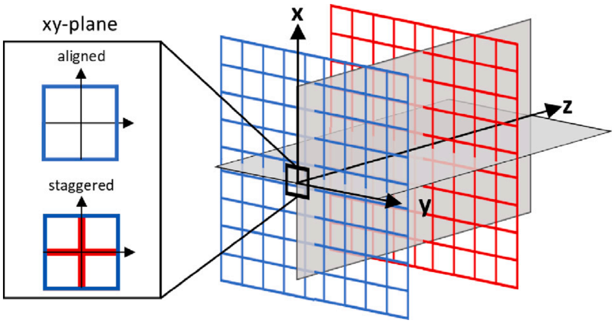

Fig. 4. Schematic illustration of the aligned (top) and staggered (bottom) multi-grid configurations viewed from the front (xy-plane). In the aligned case, consecutive grids are perfectly positioned behind one other, while in the staggered case, (one of) the next grid(s) is laterally offset (by half a cell) so that a wire crossing coincides with the center of the first grid's opening.

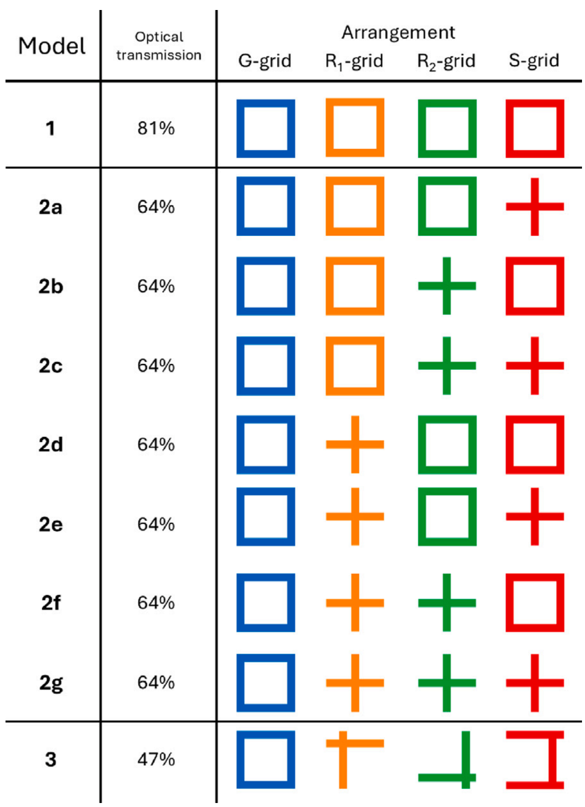

Fig. 5. Compilation of the grid configurations used in nine simulations models, viewed from the xy-plane (normal to the grid surfaces). In model 1, all grids are aligned, giving an optical transmission of 81%. In model 2, at least one of the grids is staggered relative to the entrance grids, reducing the optical transmission to 64%. Model 3 resembles the grid arrangement of the actual RFA depicted in Fig. 2 with an optical transmission of 47%.

we performed an additional simulation run (for model 1) with the nominal step length decreased to 0.1 grid unit. As can be seen in the lower panel of Fig. 3, making the trajectory integration step smaller by a factor of 10 yields no difference in the obtained results.

The exact grid configuration of the RFA (see Fig. 2) is rather complex due to a slight waviness of individual wires. In SIMION, due to the size of the computational mesh, we are limited to the use of straight grid wires. The dependence of the transmission on the alignment of the wires will be examined using several options for stacking the four grids.

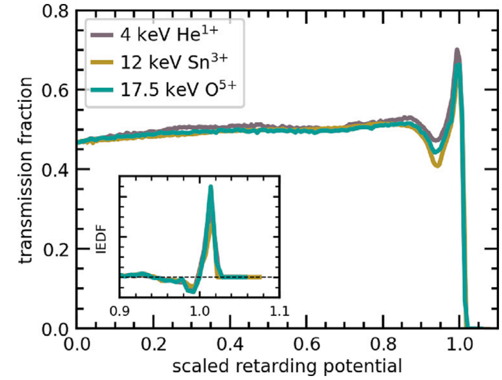

Fig. 6. Experimental transmission curves for 4 keV He^{1+}, 12 keV Sn^{3+}, and 17.5 keV O^{5+} ion beams. All exhibit the same V–I response: a slight rise in transmission followed by a pronounced dip and peak near the retarding threshold, independent of ion species, charge, or energy. This demonstrates that the transmission function is an intrinsic feature of the RFA. The inset of shows the negative derivative of the transmission curves, corresponding to the ion energy distribution functions.

The relative positioning of the individual wires is described using two classes of arrangements (see Fig. 4):

- **aligned**: this arrangement will introduce no physical ion obstruction on a consecutive grid for straight line ion trajectories.
- **staggered**: physical ion obstruction on a consecutive grid (displaced by half a cell) will occur for straight ion trajectories.

Each pair of consecutive grids can be arranged in perfect alignment or staggered. For a four-grid system, this results in eight different RFA configurations. By means of the geometrical transmission of a single grid (81%), the optical transmission for each configurations can be calculated. An overview of the eight different configurations is shown in Fig. 5, along with a ninth configuration resembling the actual RFA depicted in Fig. 2. In its second column, Fig. 5 presents the overall optical transmission and the relative positioning of each grid with respect to the entrance grid (G).

It is of note that in the present study, the possible grid configurations are limited to idealized lateral shifts between the successive grids and do not include rotation or waviness of the grid wires. Consequently, the “random” configuration considered here (model 3) does not fully capture the actual grid arrangement as shown in Fig. 2.

4. Experimental results

The ion transmission as a function of the retarding voltage has been measured for several monoenergetic ion beams. For all experimental data sets the measured I(V) curve was scaled at $V_R = 0$ V to the grid stack's optical transmission of 47% (see Section 3.2). Because different retarding voltages are required to fully stop ion beams of different energy and charge state, the retarding potential is scaled by a factor of q/E_0, which allows for a direct comparison between different ion beams.

Fig. 6 shows the experimental transmission curves for ion beams of 2 keV He^{1+} (gray), 12 keV Sn^{3+} (ochre), and 17.5 keV O^{5+} (turquoise). The same I(V) response is observed for all ion beams. As the retarding voltage is increased, the transmission fraction initially increases slightly. Below the blocking voltage of the ions, the signal exhibits a pronounced dip followed by a sharp peak. The increase in measured current is counterintuitive, since a higher potential should only reduce the transmitted ion current. The resulting dip and peak might therefore produce nonphysical features in the derived energy distribution. The

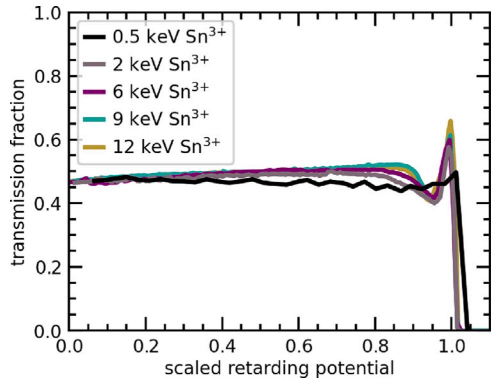

Fig. 7. Experimental transmission curves for Sn^{3+} beams at various kinetic energies. While higher-energy beams follow the characteristic transmission shape, low-energy beams show deviations caused by the stronger relative influence of the suppressor potential.

inset of Fig. 6 shows the negative derivative of the transmission curves, corresponding to the IEDF. The consistency of I(V) responses for the different ion beams indicates that the observed transmission function is a generic feature of the specific RFA used.

Fig. 7 shows the measured transmission curves for an Sn^{3+} ion beam of different energies. While the shape of the curve is retained for the highest energies, it slightly changes if the ion energy is lowered well below 1 keV. A likely explanation for this behavior lies in the fixed suppressor voltage of −100 V used throughout the measurements. The effect of the fixed suppressor voltage on the transmission function will be discussed in more detail in Section 5.2.

5. Simulation results

The following results are obtained from ion trajectory simulations of 4 keV He^{1+} ions through the different grid-model configurations illustrated in Fig. 5. Although the experimental results (Fig. 6) showed that the transmission curve is insensitive to the choice of projectile (with keV energy), using 4 keV He^{1+} in the simulations maintains consistency with the experimental dataset. A fixed suppressor voltage of −100 V is used for all simulation models, unless stated otherwise.

5.1. Perfect grid alignment (Model 1, $T_{opt} = 81\%$)

Model 1 has a grid configuration with all its grids perfectly lined up behind each other. The results of the trajectory simulations are presented in Fig. 8. The top panel of the figure depicts the fraction of ions that end up in the Faraday cup, and represents the ion transmission through the RFA. In the lower panels, each panel corresponds to a specific grid and shows the fraction of ions intercepted by that grid, i.e. the splat fraction.

The ion transmission is strongly affected by the applied retarding voltage and clearly deviates from both the single-grid transmission of 81% and the 43% calculated by the transmission multiplication rule. Over the retarding voltage range of 0 to 4 kV, the average ion transmission is 64%, as indicated by the black dashed line.

Ions flying into the detector perpendicular to the grids will only be obstructed by the first grid, the entrance grid. Therefore, when no bias is applied to any one of the grids, an ion transmission equal to the single-grid transmission of 81% is expected. This value is reproduced by the simulations. At low barrier voltages, the transmission decreases smoothly to approximately 55% at about three-quarters of the bias needed to fully block the ions. At high barrier voltages, the transmission starts to show irregular wiggles, before it fully drops to zero, see top panel of Fig. 8. The figure shows that the decreasing trend in

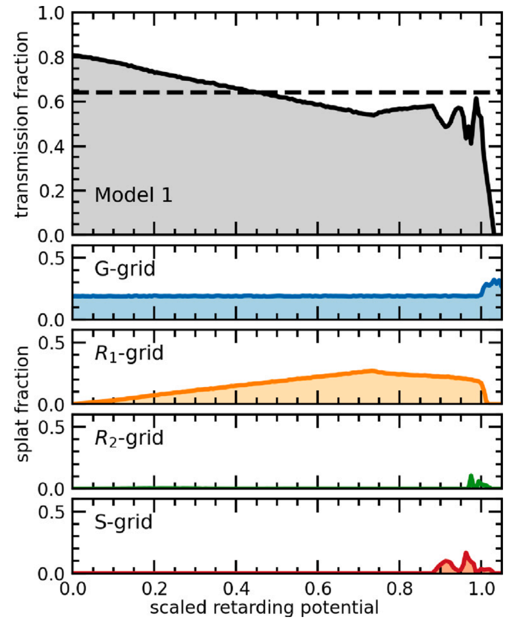

Fig. 8. Simulation results of the transmission (top row) and splat fraction (lower rows) for a 4 keV He^{1+} beam through an RFA configuration with lined up grids. The optical transmission of this model is 81%.

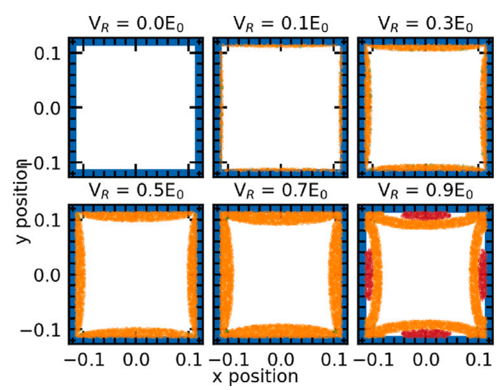

Fig. 9. Compilation of the xy-position of the 4 keV He^{1+} ions (out of the 10^5 incoming ions) which splat on either the R_1-grid (orange), R_2-grid (green), or S-grid (red), as they pass the entrance grid for different retarding voltages, as obtained from simulations using model 1. Each point represents a single splatted ion, color-coded according to the grid on which they splat. The entrance grid itself is colored in blue.

transmission is caused by an increased splatting on the R_1-grid. The wiggles are by and large related to ions hitting the suppressor grid (S-grid), and to a lesser extent the second retarding grid (R_2-grid).

For a selection of retarding voltages, the xy-positions of obstructed ions as they pass through the entrance grid are shown in Fig. 9. Each point in these figures represents a single splatted ion, color-coded according to the grid on which it splatted (see Fig. 5). It is shown that the initial smooth decrease in transmission due to an increasing number of ions splatting on the first retarding grid (R_1-grid), as shown in Fig. 8, stems from lensing effects at the entrance grid (G-grid).

5.2. Staggered grid alignments (Models 2, $T_{opt} = 64\%$)

The simulation results for staggered configurations (models 2a–g, see Fig. 5) are shown in Fig. 10. For clarity, the ion transmission (gray area) is plotted together with the splat fractions of the individual grids (colored areas). Note that all seven configurations of model 2 have the same optical transmission of 64%. To make sure that together all contributions add up to unity, the ions which at $qV_R/E_0 > 1$ get back-reflected and end up outside (O) of the RFA are represented by the purple area.

Except for configuration 2g, all transmission curves show a behavior similar to model 1: an initial decrease in ion transmission (from 64% to about 40%) followed by the occurrence of wiggles just below the drop-off voltage. Below, we discuss the recurring features in the transmission curves (Fig. 10) and relate them to the way the grids are consecutively stacked (see Fig. 5).

Low barrier voltages ($qV_R/E_0 < 0.6$)

The initial decrease in ion transmission is associated with an increased splatting on the R_1-grid (orange area) in configurations 2a–c, where R_1 is aligned with the entrance grid, as in model 1. In 2d and 2e, the R_1-grid is staggered, leading to a constant splatting fraction on R_1. The first grid aligned to the entrance grid is R_2, and accordingly the decrease in ion transmission originates from splatting on the R_2-grid. In 2f, only the suppressor (S) grid is aligned, while both retarding grids are staggered; here, the decrease in ion transmission results from increased splatting of the S-grid (red area). These findings indicate that the initial decrease in ion transmission arises whenever at least one consecutive grid is aligned with the entrance grid. The voltage at which this decreasing trend stops is determined by the distance between the entrance grid and the first aligned grid. Since the R_2-grid is positioned further downstream, and the suppressor even further, a smaller potential gradient is sufficient to produce comparable focusing and splatting effect at larger separations. In 2g, where all grids are staggered with respect to the entrance grid, no such decrease is observed.

The transmission behavior for low barrier voltages across configurations 2a–g is largely determined by which grids are aligned with the entrance grid and how subsequent grids are staggered. An initial transmission drop consistently appears whenever at least one grid is directly aligned, while configurations with all grids staggered (e.g., 2g) avoid this feature.

High barrier voltages ($qV_R/E_0 > 0.6$)

Ion splatting on the suppressor grid determines the wiggle structure in model 2a and model 2f. In these cases, the suppressor grid is staggered while the two retarding grids are aligned (see Fig. 5). For model 2a, the xy-positions of the splatted ions as they pass through the entrance grid are shown in Fig. 11 for a selection of high barrier voltages. At voltages between 80%–90% of the blocking voltage, nearly all ions not intercepted by the first retarding grid are focused onto the suppressor. This causes the ion transmission to drop to almost 0 in that voltage range.

Fig. 10 also shows that the oscillatory features in configurations 2b–e are primarily driven by splatting on the second retarding grid when it is staggered relative to the first. The oscillations are weakest in 2g, where both retarding grids and the suppressor grid are aligned. Overall, pronounced oscillations in ion transmission occur when either the second retarding grid or the suppressor grid is staggered with respect to the first retarding grid.

For high barrier voltages, the presence and strength of oscillations depends on the interplay between the retarding grids and the suppressor grid: oscillations are strongest when one of these is staggered relative to its predecessor, and weakest when they are all aligned. These general trends highlight how grid alignment governs both the baseline transmission level and the detailed shape of the transmission curves. Remarkably enough the highest and most constant transmission is found for configuration 2g (see Fig. 10) in which neither grid R_1, R_2, nor S is aligned with the entrance grid.

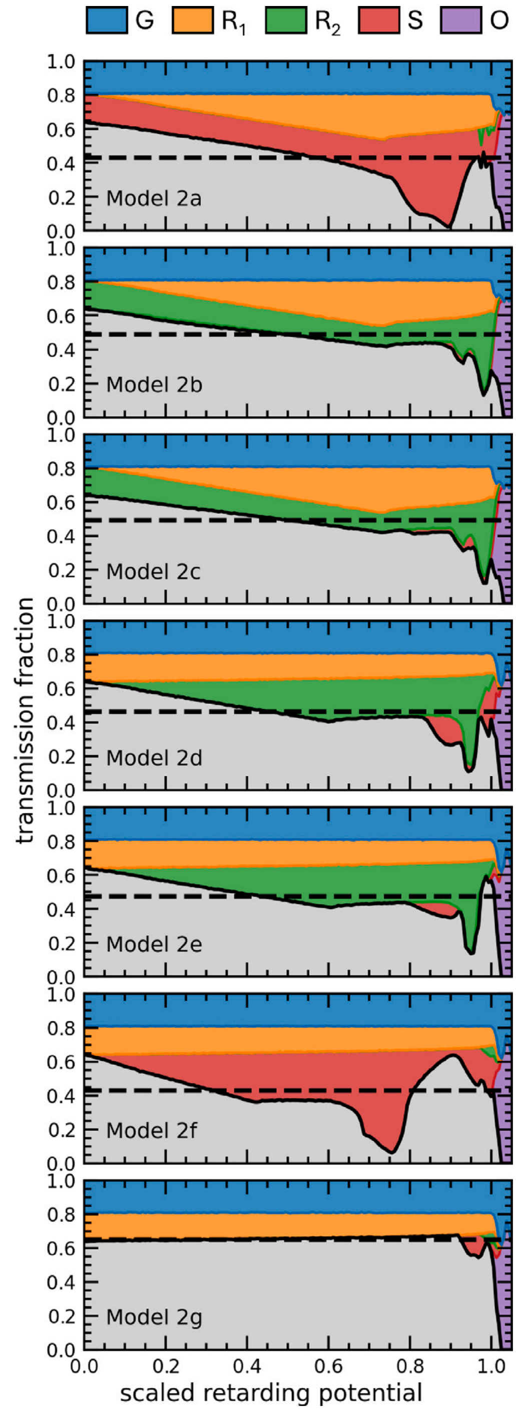

Fig. 10. Compilation of simulation results for the transmission (gray shaded area) through all the different model configurations with the same optical transmission of 64%. For each model, the fraction of the back-reflected ions that end up outside (O) of the RFA are represented by the purple areas.

The effect of the suppressor

So far, we have seen that the RFA transmission can be well represented by a single common function using a scaled argument of qV_r/E_0. However, this neglects possible effects of the suppressor voltage. The suppressor is held at a constant value in this case of −100 V, and this voltage becomes increasingly significant for lower energy beams, as was already indicated in Section 4. Using model configuration 2a, Fig. 12 (top panel) presents simulated transmission results for ions with kinetic energies from 4000 eV down to 10 eV. In addition to the

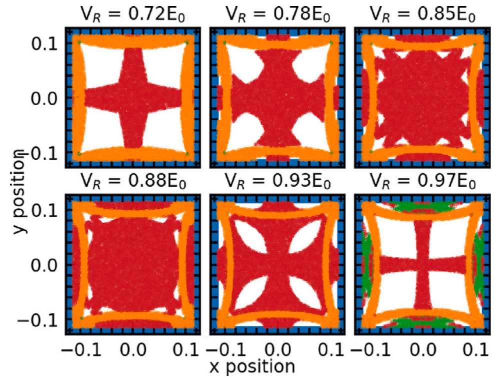

Fig. 11. Compilation of the xy-position of the ions (out of the 10^5 incoming ions) which splat on either the R_1-grid (orange), R_2-grid (green), or S-grid (red), as they pass through the entrance grid for different retarding voltages, as obtained from simulations using model 2a. Each point represents a single splatted ion, color-coded according to the grid on which they splat. The entrance grid itself is colored in blue. For these simulations a total number of 10^5 incoming ions is used.

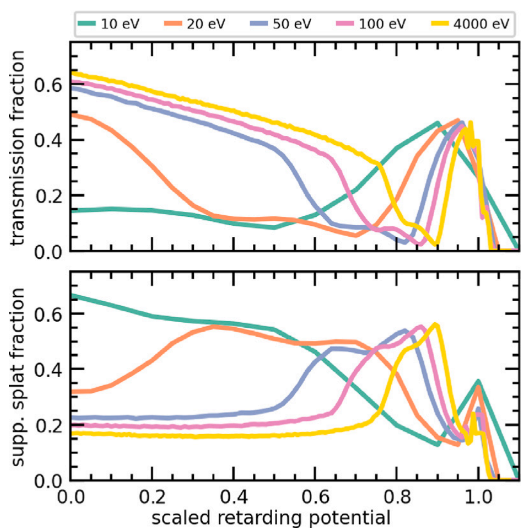

Fig. 12. Simulation results of the transmission (top panel) and splat fraction on the suppressor grid (bottom panel) for ions with energies of 4000, 100, 50, 20, and 10 eV flying through RFA model 2a. For all simulations, the suppressor voltage is −100 V.

transmission function, the splat fraction on the suppressor grid is shown to highlight its contribution.

First of all, in between qV_r/E_0 is 0.6 and 0.9 the link between decreased transmission and increased suppressor splatting is clearly visible. The precise width of the range depends on the energy of the ions: the lower the ion energy, the earlier the loss in transmission starts. In addition there is a slow shift of the transmission peak towards lower potentials with decreasing ion energy. This signals the enhanced effect of the negative suppressor voltage on the potential at the position of the second retarder grid (R_2) when the maximum retarder voltage needed to block the ions gets lower for low-energy incoming ions. Together with the suppressor voltage constituting an increasing contribution to the energy of the ions, this turns the retarder–suppressor system into a strong electrostatic lens.

In practice, this behavior implies that a fundamental trade-off in the design and operation of retarding field analyzers is required for low energy ions ($E_0 \ll$100 eV). The suppressor potential is indispensable for minimizing secondary electrons from escaping the FC. However, when

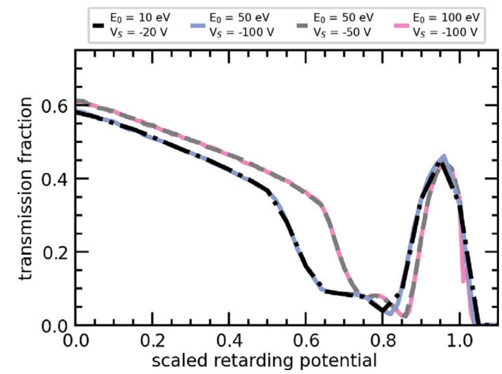

Fig. 13. Comparison of simulation transmission curves for different combinations of ion beam energy (E_0) and suppressor voltage (V_S). The curves corresponding to $V_S = -100$ V are identical to those shown in Fig. 12 and are included here for direct comparison of similar $|qE_0/V_S|$ values.

kept constant at a relatively high value, it can disproportionately affect the transmission of low-energy ions. As a rule of thumb, Fig. 12 suggests that if $|qE_0/V_s| > 1$, the effect is not yet significant.

At smaller ratios of $|qE_0/V_s|$ the common transmission curve needs to be adjusted or one needs to accept that the absolute current measurement is slightly higher due to secondary electrons escaping from the FC. This effect is likely negligibly small as for low-energy ions and in particular for singly charged ions the secondary electrons have energies well below 20 eV. For low-energy measurements, a suppressor voltage of −100 V is therefore typically not needed. We investigated whether similar transmission curves are obtained for identical $|qE_0/V_s|$ ratios at lower ion beam energies and correspondingly reduced suppressor voltages. Fig. 13 compares the cases of 50 eV and 100 eV ion beams with a suppressor voltage of −100 V (corresponding to $|qE_0/V_s|$ ratios of 0.5 and 1, respectively), as presented in Fig. 12, with the combinations of 10 eV and −20 V ($|qE_0/V_s| = 0.5$) and 50 eV with −50 V ($|qE_0/V_s| = 1$). It is observed that the transmission curves overlap closely when the same $|qE_0/V_s|$ ratio is maintained, indicating that the transmission behavior is primarily governed by this ratio rather than the absolute suppressor voltage.

5.3. Random grid alignment (Model 3, $T_{opt} = 47\%$)

Model 3 has a grid configuration that resembles the actual RFA shown in Fig. 2. None of the grids are either aligned nor staggered with respect to the entrance grid. The results of the trajectory simulations are shown in Fig. 14.

From the figure it is seen that now with the grids arranged randomly rather than in a strictly aligned or staggered manner, the transmission curve becomes noticeably flatter. No single grid dominates the loss of ions by splatting, and their contributions are more evenly spread out over the retarder voltage range. Consequently, the characteristic initial drop and oscillatory structures seen in the ordered configurations are largely suppressed. This suggests that randomization effectively averages out the grid-specific effects, leading to a smoother and more uniform transmission behavior. These findings are consistent with the experimental results shown in Fig. 6, which exhibit only a slight change in transmission at low barrier voltages. However, the pronounced dip and peak present in the experimental figures are not reproduced by the simulations. This discrepancy may partly arise from the simplified nature of the simulation model with randomly aligned grids, which only approximates the complex grid stack configuration illustrated in Fig. 2.

In addition, another factor might be beam divergence. The maximum angle defined by the collimating diaphragms in our experimental setup is approximately 1°. To assess the effect of a small inclination

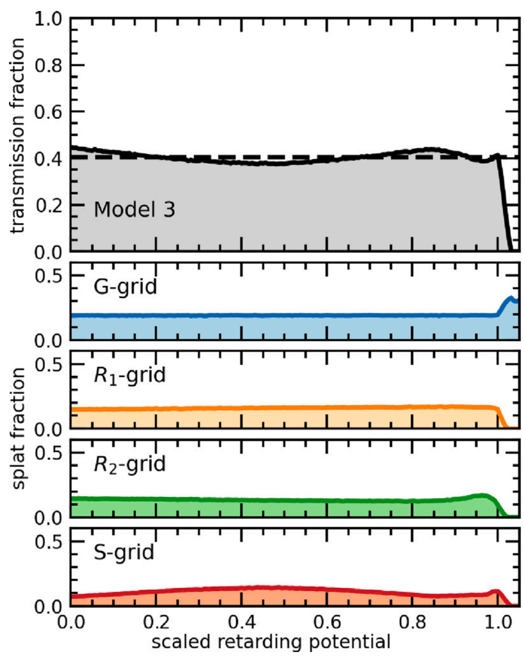

Fig. 14. Simulation results of the transmission (top row) and splat fractions (lower rows) for ions through a model that resembles the actual RFA used in our experiments (see Fig. 2). The optical transmission of this stack configuration is 47%.

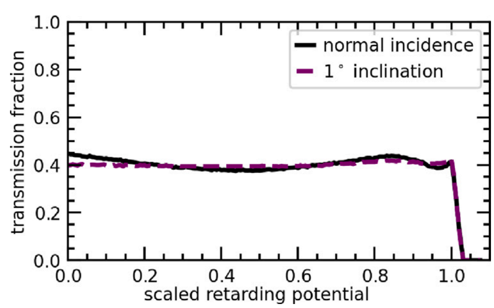

Fig. 15. Simulated transmission characteristics for the "random" grid configuration (model 3) for a 4 keV He^{+} ion beam at normal incidence (black solid line) and at 1° inclination (purple dashed line) with respect to the grid normal.

angle of the incoming beam, an additional simulation was performed and is shown in Fig. 15. It appears that the inclusion of a small inclination angle in the incoming beam even further flattens the transmission curve.

Both non-ideal alignment and beam divergence have the tendency to flatten the transmission curve of an RFA, implying that RFA design should not aim for perfect grid alignment. This complements the work of Trottenberg et al. [23] who reached the same conclusion for rotational grid alignment of grids with circular holes.

6. Conclusion

In this work, the voltage-dependent transmission of a four-grid retarding field analyzer has been investigated through a combination of monoenergetic ion-beam experiments and detailed ion-trajectory simulations. Experimentally, all investigated ion species and charge states experience the same characteristic transmission-voltage response when the retarding voltage is scaled by qV_R/E_0, demonstrating that the observed behavior is an intrinsic property of the analyzer rather than a feature of the incoming beam. Initially, the transmission changes only weakly with retarding voltage, followed by a pronounced dip and sharp peak just below the cutoff voltage. At lower ion energies, deviations from this universal curve occur due to the increasing relative influence of the fixed suppressor potential.

The simulations reproduce the essential features of the measured transmission curves and provide a physical explanation of their origin. They show that the transmission is affected by electrostatic lensing effects arising from the grid apertures and their relative alignment. As a retarding voltage is applied, these lensing effects slightly bend ion trajectories in particular the ones passing through the grid near the grid wires. This enhances the probabilities of interception by the subsequent grid(s). Which one of the grids that dominates the ion loss depends on the relative alignment of consecutive grids. In particular, aligned grid pairs promote voltage-dependent focusing that leads to systematic transmission losses, while staggered or randomly aligned configurations tend to suppress such effects.

Near the cutoff voltage, the suppressor grid plays a decisive role in shaping the transmission function. For certain grid configurations, ions that pass the retarding grids are strongly focused onto the suppressor, producing oscillatory features in the transmission curve. These oscillations are most pronounced when the suppressor or second retarding grid is staggered with respect to its predecessor. At low ion energies, the fixed suppressor voltage significantly alters the effective retarding field, shifting and distorting the transmission curve and imposing practical constraints on absolute flux measurements.

Overall, the results demonstrate that RFA transmission cannot be adequately described by simple optical transparency estimates or by multiplicative transmission rules. Instead, transmission is a voltage-dependent function determined by an interplay of grid geometry, alignment, spacing, and electrode biasing. Accurate quantitative interpretation of RFA measurements therefore requires explicit considerations of this transmission function, particularly when deriving the ion energy distribution function or measuring absolute ion fluxes. These findings underscore the importance of analyzer specific calibration or simulation-based correction methods and provide clear guidelines for the design and operation of RFAs with improved and more stable transmission characteristics.

CRediT authorship contribution statement

L. Assink: Writing – original draft, Visualization, Software, Methodology, Investigation, Formal analysis, Data curation, Conceptualization. **E. de Wit:** Writing – review & editing, Investigation. **F. Veen:** Writing – review & editing, Visualization, Investigation. **K. Bijlsma:** Writing – review & editing, Investigation. **O.O. Versolato:** Writing – review & editing, Supervision. **R. Hoekstra:** Writing – review & editing, Writing – original draft, Supervision, Resources, Project administration, Conceptualization.

Declaration of competing interest

The authors declare that they have no known competing financial interests or personal relationships that could have appeared to influence the work reported in this paper.

Acknowledgments

This work was conducted as part of the research program of the Advanced Research Center for Nanolithography (ARCNL), a public–private partnership of the University of Amsterdam (UvA), Vrije Universiteit Amsterdam, University of Groningen (RuG), the Netherlands Organisation for Scientific Research (NWO) and the semiconductor equipment manufacturer ASML. The experiments were performed at the ZERNIKELEIF facility operated by the Zernike Institute for Advanced Materials at the University of Groningen.

Data availability

Data will be made available on request.

References

[1] W.B. Hanson, D.R. Zuccaro, C.R. Lippincott, S. Sanatani, The retarding-potential analyzer on atmosphere explorer, Radio Sci. 8 (1973) 333–339.

[2] R.A. Pitts, R. Chavan, S.J. Davies, S.K. Erents, G. Kaveney, G.F. Matthews, G. Neill, J.E. Vince, Retarding field energy analyzer for the JET plasma boundary, Rev. Sci. Instrum. 74 (2003) 4644–4657.

[3] D. Gahan, B. Dolinaj, M.B. Hopkins, Retarding field analyzer for ion energy distribution measurements at a radio-frequency biased electrode, Rev. Sci. Instrum. 79 (2008) 033502.

[4] F. Schlichting, H. Kersten, A redarding field thermal probe for combined plasma diagnostics, EPJ Tech. Instrum. 10 (2023).

[5] S.W. Tang, W. Gekelman, Design of a retarding field energy analyzer for the large plasma device, EPJ Tech. Instrum. 52 (2024).

[6] S. Kagaya, H. Takahashi, T. Seino, K. Yoshimura, R. Nishimura, A. Kanno, Y. Takahashi, T. Hara, T. Oishi, A. Matsuyama, K. Tobita, Determination of parallel and perpendicular ion temperatures based on selective ion transmission in a retarding field analyzer, Plasma Fusion Res. 19 (2024) 1201021.

[7] Y. Damizia, S. Elmore, P. Ryan, S. Allan, F. Federici, N. Osborne, J.W. Bradley, The MAST-U Team, First ion temperature measurements in the MAST-U divertor via retarding field energy analyzer, Nucl. Mater. Energy 43 (2025) 101912.

[8] B. Zhao, D.C. Donovan, J. Ren, M.D. Phillips, Novel data interpretation method for DIII-D divertor retarding field energy analyzer with 3-D particle-in-cell simulations, Rev. Sci. Instrum. 95 (2024) 073512.

[9] K.I. Bijlsma, L. Oltra, E. de Wit, L. Assink, I. Rabadán, L. Méndez, R. Hoekstra, Electron capture from molecular hydrogen by metastable sn^{2+*} ions, Atoms 12 (2024) 9.

[10] P.K. Saha, D. Roy, M. Chakraborty, Generation of supersonic ion beams in the down stream of mulitple double layer, Phys. Lett. A 545 (2025) 130486.

[11] S. Balachandran Nair, A. Chandrika Sreekantan, R. Sudharshan Kaarthik, Metrological evaluation of a programmable gain current-sensing digitizer suitable for retarding potential analyzers, IEEE Sens. J. 23 (2023) 29073–29083.

[12] A. Caldarelli, F. Filleul, R. Boswell, C. Charles, N. Rattenbury, J. Cater, Data processing techniques for ion and electron-energy distribution functions, Phys. Plasmas 30 (2023) 040501.

[13] A. Caldarelli, R. Andriulli, F. Ponti, J. Cater, N. Rattenbury, Effect of input power on plasma expansion and ion acceleration in a radio-frequency plasma thruster, Acta Astronaut. 226 (2025) 521–530.

[14] A. Thomas, K. Lemmer, Time-resolved ion energy measurements using a retarding potential analyzer for electric propulsion applications, Rev. Sci. Instrum. 95 (2024) 023505.

[15] L. Poirier, A.C. Lassise, R. Hoekstra, J. Sheil, O.O. Versolato, Laser-intensity dependence of ion emission from Nd:YAG-laser-produced plasma expanding into vacuum, Phys. Plasmas 30 (2023) 083505.

[16] S. Rai, K.I. Bijlsma, L. Poirier, E. de Wit, L. Assink, A.C. Lassise, I. Rabadan, L. Mendez, J. Sheil, O.O. Versolato, R. Hoekstra, Evidence of production of kev Sn^{+} ions in the H_2 buffer gas surrounding a Sn-plasma EUV source, Plasma Sources Sci. Technol. 32 (2023) 035006.

[17] J. Sheil, L. Poirier, A.C. Lassise, S. Schouwenaars, N. Braaksma, A. Frenzel, R. Hoekstra, O.O. Versolato, Power-law scaling relating the average charge state and kinetic energy in expanding laser-driven plasmas, Phys. Rev. Lett. 133 (2024) 125101.

[18] Y. Sakai, I. Katsumata, An energy resolution formula of a three plane grids retarding field energy analyzer, Japan. J. Appl. Phys. 24 (1985) 337–341.

[19] D. Gahan, B. Dolinaj, M.B. Hopkins, Comparison of plasma parameters determined with a langmuir probe and with a retarding field energy analyzer, Plasma Sources Sci. Technol. 17 (2008) 035026.

[20] T. Baloniak, R. Reuter, C. Flötgen, A. von Keudell, Calibration of a miniaturized retarding field analyzer for low-temperature plasmas: geometrical transparency and collisional effects, J. Phys. D: Appl. Phys. 43 (2010) 055203.

[21] K. Denieffe, C.M.O. Mahony, P.D. Maguire, G. D., M.B. Hopkins, Retarding field energy analyser ion current calibration and transmission, J. Phys. D: Appl. Phys. 44 (2011) 075205.

[22] T.H.M. van de Ven, C.A. de Meijere, R.M. van der Horst, M. van Kampen, V.Y. Banine, J. Beckers, Analysis of retarding field energy analyzer transmission by simulation of ion trajectories, Rev. Sci. Instrum. 89 (4) (2018) 043501.

[23] T. Trottenberg, F. Bansemer, M. Hesse, H. Kersten, J. Laube, V. Schneider, B. Schuster, L. Seimetz, R.F. Wimmer-Schweingruber, The role of grid geometry and relative orientation in the performance of a retarding potential analyzer, AIP Adv. 15 (2025) 035030.

[24] J.H. Klenzing, G.D. Earle, R.A. Heelis, Errors in ram velocity and temperature measurements inferred from satellite-borne retarding potential analyzers, Phys. Plasmas 15 (2008) 062905.

[25] K. Bijlsma, E. de Wit, J.L. Pascual, E. Kleinsmit, L. Assink, M. Salverda, L. Méndez, O.O. Versolato, I. Rabadán, R. Hoekstra, Electron capture in low-energy collisions of $Sn^{3}+$ ions with H_2 and D_2, Phys. Rev. A 112 (2025) 052806.

[26] G. Lubinski, Z. Juhász, R. Morgenstern, R. Hoekstra, State-selective electron-capture cross section measurements for low-energy collisions of He-like ions on H_2, J. Phys. B: At. Mol. Opt. Phys. 33 (2000) 5275—-5296.

[27] R. Geller, Electron Cyclotron Resonance Ion Sources and ECR Plasmas, Springer-Verlag GmbH, 1996.

[28] O.O. Versolato, J. Sheil, S. Witte, W. Ubachs, R. Hoekstra, Microdroplet-tin plasma sources of EUV radiation driven by solid-state-lasers, J. Opt. 24 (2022) 054014.

[29] D.A. Dahl, J.E. Delmore, A.D. Appelhans, SIMION PC/PS2 electrostatic lens design program, Rev. Sci. Instrum. 61 (1) (1998) 607.

[30] D.A. Dahl, SIMION for the personal computer in reflection, Int. J. Mass Spectrom. 200 (1–3) (2000) 3–25.